RESEARCH PAPER

Macroscale friction of granular soils under monotonic and cyclic loading based upon micromechanical determination of dissipated energy

Daniel H. Johnson[1] · Farshid Vahedifard[2] 🄳 · John F. Peters[1]

Abstract

Macroscopic frictional behavior of granular materials is of great importance for studying several complex problems associated with fault slip and landslides. The main objective of this study is to model the macroscale frictional behavior of granular soils under monotonic and cyclic loadings based upon micromechanical determination of dissipated energy at particle contacts. This study is built on the general observation that the externally computed energy dissipation should be equal to the total internal energy dissipation derived from inter-particle sliding and rolling, energy losses from inter-particle collisions, and damping. For this purpose, the discrete element method is used to model a granular soil and determine the stored, dissipated, and damping energies associated with shear loading for applied monotonic and cyclic velocities. These energies are then related to the friction by an application of the Taylor-critical state power balance relationship. Also, the contributions of the different modes of energy dissipation (normal, shear, and rolling) to the total frictional resistance were studied. By changing the inter-particle friction, the simulations showed that the macroscopic friction was nearly constant, the slip friction increased almost linearly with increasing inter-particle friction, and the difference between the two was attributed to the non-energy dissipating dilatancy component. By providing a clear relationship between energy dissipated by micro-scale mechanisms versus the traditional engineering definition based on macro-scale (continuum) parameters, this study provides a means to develop a better understanding for the frictional behavior of granular media.

Keywords Discrete element method · Dissipated energy · Friction · Granular soils · Micromechanics

1 Introduction

The frictional behavior of granular systems is critical to engineering behavior for many rock and soil mechanics applications. In particular, frictional behavior is a key mechanism in understanding the initiation of fault motions leading to earthquakes where energy is released quickly from shearing motion in localized zones. The mechanical properties of rocks in gouge zones play a crucial role in the source mechanisms of earthquakes, in particular the frictional properties of the fault gouge [4]. Such problems involve not only the mechanical role of friction, but also the thermo-mechanical coupling associated with rapid shearing in localized zones. A number of laboratory experiments have been conducted to observe macro-scale friction for earthquakes (e.g., [1, 13, 14, 23, 24, 32]). Similar problems emerge in understanding the role of friction in relative motion between soils and construction materials [8, 29, 42, 55, 57, 67, 70] and in landslides [6]. For granular materials, the macroscale frictional behavior is of great importance and is shown to relate to microscale energy dissipation [2, 19, 22, 30, 36, 45, 46, 53, 58, 61, 66].

✉ Farshid Vahedifard
farshid@cee.msstate.edu

Daniel H. Johnson
dhj21@cavs.msstate.edu

John F. Peters
particledad@gmail.com

[1] Center for Advanced Vehicular Systems (CAVS), Mississippi State University, Mississippi State, MS 39762, USA

[2] Richard A. Rula School of Civil and Environmental Engineering, Mississippi State University, Mississippi State, MS 39762, USA

Observations thus far stress the complexity and diversity of friction phenomena in rock and soil mechanics [4].

The majority of constitutive models for granular materials, such as Mohr–Coulomb and rate-and-state frictional models, are based on the macroscopic frictional characteristics of granular materials [15]. The relationship between the macroscopic frictional behavior and the inter-particle friction has been investigated extensively through experiments [49] and numerically using the discrete element method (DEM) (e.g., [27, 50, 54]). A general finding emerging from these studies is a seeming lack of correspondence between the measured macroscale frictional behavior and the inter-particle friction. The main challenge in such studies is the difficulty in relating microscale parameters such as contact friction and damping to the measured macroscale parameters. For example, DEM simulations of the direct shear tests show that the macroscale friction of spheres depend on inter-particle friction for values of less than 0.35. However, for interparticle friction values greater than 0.35, the macro-scale response is not sensitive to inter-particle friction [9, 54]. Similarly, several studies (e.g., [33, 34, 44]) showed that the macroscopic frictional behavior depends on the shape of particles. In addition to the Coulomb friction shearing granular zones dilate, thus causing resistance to shear through a transfer of stress to the direction normal to shearing motion. The distinction between the two resistance mechanisms becomes important when considering heat generation within the zone because whereas heat is generated by frictional energy dissipation, the resistance derived from dilatancy is through an energy transfer between shear and normal deformation modes that does not contribute to energy dissipation. To fully understand important energy mechanisms, therefore, special attention must be paid to particle-scale mechanics.

For continuum constitutive models, such as rate-and-state friction models, macroscopic frictional behavior is a key parameter. For example, for fault slip modeling, the macroscopic friction coefficient was shown to greatly depend on the rate of fault slip. In certain cases, the magnitude of the friction coefficient could greatly increase (velocity-strengthening) or decrease (velocity-weakening), depending on the slip rate [43]. Rate and state friction models have been used in the area of frictional weakening of slip interfaces [63]. Comparisons between microphysical models and rate and state models have been studied [7, 11, 20]. The DEM has the potential for a microphysical interpretation of rate-and-state friction as described by van den Ende et al. [12], who investigated effects on the transient and steady state macroscopic frictional behavior of a system. The DEM has also been used to study energy dissipation in soil samples and other granular materials (e.g., [17, 62, 68, 69]). Additionally, in recent works, the DEM has been coupled with fluid solvers to model the micromechanics involved in piping erosion [51], seepage induced erosion [16], and hydraulic fracturing of rocks [28, 56]. Alternatively, the DEM was used to understand the effects of details such as the effect of size and shape of the grains on the macroscopic frictional behavior [33] and the effect of inter-particle friction on the macroscopic frictional behavior [27]. Additionally, Morgan [35] used a particle dynamics method to investigate the sliding friction, slip friction, and inter-particle friction for shear slip.

This study focused on DEM simulations using spherical unbonded particles. However, the general approach described here can be extended to different settings including non-spherical particles, bonded particles, contact degradation, and particle breakage. These mechanisms can change the frictional behavior of the particle contacts [26]. As a group, methods involving localized slip in earthquake and landslide mechanics are characterized by very large strains, in contrast to the majority of engineering applications for granular media occurring at small strains, especially for motion in fault gouges (e.g., [35]), landslides (e.g., [66]) and shear-thickening fluid (e.g., [5]). The strain can be as great as 150% for the commonly used two-dimensional (2D) idealizations (e.g. [35]).

The main objective of this study is to predict the macroscale frictional behavior of granular soils under static and cyclic loading based upon micromechanical determination of dissipated energy at particle contacts. The study is built on the general observation that the externally computed energy dissipation should be equal to the total internal energy dissipation derived from inter-particle sliding and rolling, energy losses from inter-particle collisions, and damping. For this purpose, we use the DEM to model a granular soil and determine the stored, dissipated, and damping energies associated with shear loading for static and cyclic loading conditions. The relationship between the internal energy dissipation and macro-scale friction is determined through a simple interpretation of the critical state power relationship [47, 52, 65]. One unique aspect of the study is use of a detailed accounting of the energy balance at the particle scale, thus providing context to the relationship between measured internal dissipation rate and the friction inferred from boundary measurements. The ability to measure energy dissipation based on local measurements is important in future thermodynamic analysis of heat flow within shearing granular masses. Given the independent determination of macroscale friction caused by particle-scale forces, the effect of dilation is described by observing the differences in the macroscale friction and the slip friction that is measured based on stresses measured at the boundaries. Also, the contributions of the different modes of energy dissipation (normal, shear, and rolling) are studied. The following sections briefly discuss

the DEM, the energy method being used, the numerical model boundary conditions and initial parameters. Following the numerical model, the results are presented and then discussed.

2 Theory and formulation

2.1 Frictional components and energy dissipation in granular media

Monitoring the amount of energy in a system improves the understanding of how the particles at the microscale interact and affect the behavior at the macroscale. The macroscopic friction generated by particle interaction is proportionate to the amount of energy the system dissipates with respect to the applied stresses. The slip friction of the system is defined by the ratio of the shear stress and normal stress at the loading boundary. Since the outer boundaries of the system are allowed to move, the system can either dilate or compress, which leads to a dilative component of friction. Figure 1 provides a visual description of the variables used in the energy calculations.

For simple shear loading, the slip friction of the system can be defined in terms of the stresses at the limit state as:

$$\mu_s = \frac{\tau}{\sigma_n} \tag{1}$$

where μ_s is the slip friction, τ is the shear stress, and σ_n is the normal stress, both stresses acting on the top boundary of the specimen. The total work rate (power) input to the

Fig. 1 Domain showing applied boundary conditions where σ_n is the normal stress applied, τ is the shear stress applied, v_s is the velocity in the horizontal direction, and v_n is the velocity in the vertical direction. The cross-sectional area in Eq. (3) is defined as, $A_s = L \times b$. Note the in-depth (z-direction) has a plane strain boundary condition applied, and the shear direction has a periodic boundary condition

layer is given unambiguously as the product of the surface velocities and forces:

$$\dot{W}_s = F_s v_s + F_n v_n \tag{2}$$

where $\dot{W}_s$ is the total power to the system, F_s is the shear force, v_s is the shear velocity, F_n is the normal force, and v_n is the normal velocity. The power can be expressed as a specific power, or power per volume of specimen, as:

$$\dot{W}_v = \frac{1}{hA_s}(F_s v_s + F_n v_n) = \tau\dot{\gamma} + \sigma_n\dot{\epsilon}_n \tag{3}$$

where $\dot{W}_v$ is the total power per volume of the system, h is the thickness, A_s is the cross-sectional area, $\dot{\gamma}$ is the average shear strain rate, and $\dot{\epsilon}_n$ is the average normal strain rate.

The specific power can be related to the internal energy dissipated though a computation of the total energy balance in the layer of discrete elements taking into account the kinetic energy of the particles and the energy stored and dissipated at particle contacts. In that case, $\dot{W}_v$ is a measured quantity. The internal dissipation rate can also be expressed as a phenomenological law, as in the case of the Taylor [52] energy law used in the Critical State Soil Mechanics theory [47, 52, 65]:

$$\dot{W}_v = \mu_e \sigma_n \dot{\gamma} \tag{4}$$

where μ_e is the frictional component of macroscopic dissipated energy. By combining Eqs. (3) and (4) and rearranging terms, the stress-dilatancy equation is obtained:

$$\frac{\dot{\epsilon}_n}{\dot{\gamma}} = \mu_e - \frac{\tau}{\sigma_n} \tag{5}$$

Equation (5) states that the rate of dilation/contraction is the difference of the stress ratio, τ/σ_n, and the macroscopic friction, μ_e. The characteristic stress ratio, μ_e, can also be obtained from the internal energy rate in light of Eq. (4):

$$\mu_e = \frac{1}{\sigma_n} \frac{dW_v}{d\gamma} \tag{6}$$

The friction resistance observed externally is given by $\mu_s = \tau/\sigma_n$, and the dilation/contraction friction can be expressed by $\mu_d = \dot{\epsilon}_n/\dot{\gamma}$. These terms can be applied to the stress-dilatancy equation (Eq. 4) to obtain:

$$\mu_e = \mu_d + \mu_s \tag{7}$$

where μ_d is the dilative component of friction. Note, that with the compression-positive sign convention used in this work, μ_d is negative when the granular layer is dilating. Equation (7) implies when the rate of volume change is zero, such as at the critical state, $\mu_e = \mu_s$. Use of Eq. (4) is a foundational idea of Critical State Soil Mechanics. In this work, application of Eq. (6) is based on computing $dW_v/d\gamma$ internally as the summation of contribution of all particle contacts.
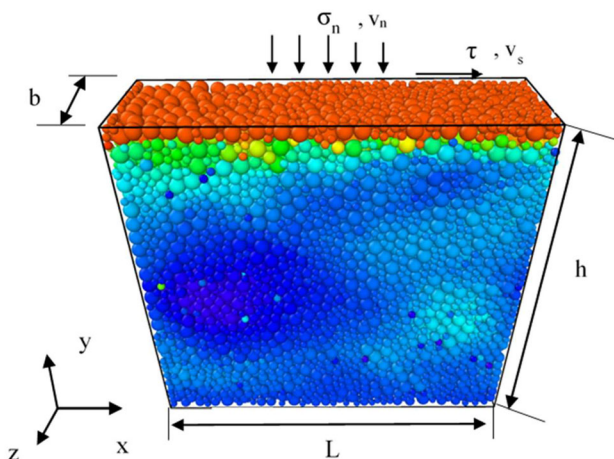
2.2 Energy calculations in DEM

The DEM [10] is a numerical method used for simulating interacting bodies by integrating the equations of motion for each body. Contact laws define forces and moments created by relative motions of the particles describe the interactions between particles. These forces are based on the relative displacement of the bodies (particles) at the point of their contact. The particles are assumed to be rigid. The DEM is designed to simulate granular media in large assemblages, ranging from a few thousand particles to millions of particles. To simplify the contact detection in the DEM, the particles are considered to be spherical in the current study. Spherical particles are used as a computational expedient; non-spherical particles can be modeled, although at the expense of added memory usage to describe particle geometry and added computational time for contact detection. By using the rolling resistance parameter, the spherical particles can better approximate the behavior of non-spherical particles and more realistically simulate the microstructure of shear bands [21]. Peters et al. [39] provide a general philosophy of using spherical particles with rolling resistance for prototype-scale simulations.

DEM models are shown to provide robust tools for micromechanical and prototype-scale simulations of complex phenomenon in granular media (e.g., [39]). Among others, DEM modeling has been used for energy dissipation calculations for granular soils such as dissipated energy of the system for cyclic loading cases [48]. More recently, the DEM has been used to study fracture growth [59]. To expand these previous DEM energy works, this study calculates each specific mode of energy dissipation (normal, shear, rolling, and damping) to determine the macroscopic friction. After determining these energies, the macroscopic friction of the system is determined by using Eq. (6), where W_v is determined by the dissipated energy of the system.

The particle acceleration is computed from the summation of contact forces acting on each particle combined with external forces. The motion of each particle that results from the net forces and moments is obtained by integrating Newton's laws. The evolution of particle velocity, v_i and rotational rate ω_i are given by:

$$m \frac{\partial v_i}{\partial t} = m g n_i^g + \sum_{c=1}^{N_c} f_i^c \tag{8}$$

and

$$I_m \rho \frac{\partial \omega_i}{\partial t} = \sum_{c=1}^{N_c} e_{ijk} f_j^c r_k^c + \sum_{c=1}^{N_c} M_i^c \tag{9}$$

where m and I_m are the particle mass and moment of inertia respectively, $g n_i^g$ is the acceleration of gravity, f_i^c and M_i^c

are the forces and moments applied at the contacts, ρ is the particle density, r is the particle radius, e_{ijk} is the permutation tensor, and N_c is the number of contacts for the particle.

Particle forces are accumulated from pairwise interactions between particles. Two particles with radii R_A and R_B make contact when the distance, d, separating the particles satisfies

$$d < R_A + R_B \tag{10}$$

The contact forces and moments arise from relative motion between contacting particles. The motion of each individual particle is described by the velocity of the particle center and the rotation about the center. The branch vector between sphere centers, $x_i^A - x_i^B$ is also the difference between the respective radii vectors that link the particle centers to the contact $r_i^A - r_i^B$. With this nomenclature, the relative motion at contact c between particles A and B is given by:

$$\Delta_i^c = u_i^A - u_i^B + e_{ijk} \left(r_j^A \theta_k^A - r_j^B \theta_k^B \right) \tag{11}$$

where Δ_i^c is the displacement of the contact, u is the displacement of each particle, r is the radius of the particle, and θ is the angular displacement, and the repeated indices indicate summation. The contact moments are generated by the difference in rotations, $\Delta \omega_i^c$, between the particles A and B,

$$\Delta \omega_i^c = \omega_i^A - \omega_i^B \tag{12}$$

where ω is the angular velocity of the particle. The contact forces and moments for cohesionless materials are given by the contact laws in terms of their normal and shear components, f^n, and f_i^s and the moment term M_i^c,

$$f^n = \begin{cases} K^n \Delta^n \\ E_r K^n (\Delta^o - \Delta^n), & \Delta^n < \Delta^o \end{cases} \tag{13}$$

$$f_i^s = \begin{cases} K^s \Delta_i^s \\ f^n \tan \phi n_i^s, & |f_i^s| \geq f^n \tan \phi \end{cases} \tag{14}$$

$$M_i^c = \begin{cases} K^r \Delta \omega_i^c \\ f^n \tan \phi_m n_i^m, & |m_i^c| \geq f^n \tan \phi_m \end{cases} \tag{15}$$

where K^n, K^s, and K^r are stiffness constants, where the unit of K^r is N-m; E_r is a factor to control energy dissipation through stiffening the unload response [60]; Δ^n and Δ_i^s are the normal and shear components of the contact displacement; n_i^s and n_i^m are the unit vectors in the direction of the shear force and moment; Δ^o is the greatest value of penetration in the history of Δ^n; and ϕ and ϕ_m are friction angles. The inter-particle friction (μ_p) and rolling friction (μ_r) parameters are directly determined from ϕ and ϕ_m, respectively. At the microscale, the static and dynamic frictions are not distinguished in the application of the

friction coefficient. The sliding and rotational modes amount to an elastic–plastic law that dissipates energy through Coulomb friction. In all three modes, there can be force–displacement states that lie on the unload-reload portions of the response. These are not easily damped by hysteretic mechanisms without adding complexity and additional internal variables. For this unload–reload state damping is invoked that eliminates high-frequency vibrations, but without introducing significant rate-dependence. For Eq. (14), the condition $f_i^s \geq 0$ is invoked. Interested readers are referred to Johnson et al. [25] for further details about the DEM formulations used in this study.

It is well known that forces are transmitted through meso-scale structures referred to as force chains. Peters et al. [40] provide an objective statistical technique for identifying particles participating in force chains. In this work force chains will be subjectively identified through looking at patterns of particle stress. The particle stress tensor and the average continuum stress in the solid fraction are defined as [31, 37, 38]:

$$\sigma_{ij}^p = \frac{1}{V_p} \sum_{c=1}^{N^c} r_i^c f_j^c \tag{16}$$

$$\overline{\sigma}_{ij} = \frac{1}{V} \sum_{p=1}^{N^p} V_p \sigma_{ij}^p = \frac{V_s}{V} \sigma_{ij}^p \tag{17}$$

where V is the total volume, V_p is the volume of each particle, V_s is the total particle volume, N^c is the number of contacts, N^p is the number of particles, f_i^c is the ith component of the force acting at the contact, and r_j^c is the jth component of the radius vector from the center of the particle to the contact. The particle stresses can be used to identify the particles transmitting higher than average loads through force chains. A visual inspection of particles groups having high principal stresses is a simple way to subjectively identify force chains.

We calculate different types of energy including the kinetic, stored, dissipated, and damping energies. The stored and kinetic energies represent the current energy state of the particles; whereas, the dissipated and damping values represent a rate of energy leaving the system through contact interactions. For each simulation, an energy balance was conducted to verify that the output energy and input energy were equal at all times. For this, the output energy is a summation of the kinetic, dissipated, and damping energy, and the input energy is determined based on the applied strain rate to the boundary of the shearing layer. It should be noted that in these simulations, the stored energy component was much smaller than the other components and considered negligible. In addition, the dissipated and damping energies have components of normal, shear, and rolling.

Figure 2 shows an example of the force–displacement curves for individual contacts. The hysteretic components of dissipated energy are determined by finding the area of the shaded region under the curves, as expressed in Eqs. (18–24). Considering the normal contact, the stored normal energy is determined by the area in Fig. 2a, the dissipated normal energy is determined by the area in Fig. 2b, and the damped normal energy is determined similar to the dissipated energy. For the normal contact shown in Fig. 2a, the contact response is essentially that of an elastic–plastic mechanism in which the *inelastic strains occur during the loading increase*, making the unloading an elastic response. Accordingly, the stored energy is that retrieved when unloading is given by the area of the triangle made by the unload curve. This reasoning is illustrated clearly for the shear and rotational response shown in Fig. 2c, where, again, the stored energy represents the energy that would be recovered upon unloading. Therefore, the normal and shear components of the stored energy can be given by:

$$E_{\text{Stored}}^{\text{n}} = \frac{1}{2} \delta_t^2 K_t = \frac{1}{2} \delta_t f_{\text{n}} \tag{18}$$

$$E_{\text{Stored}}^{\text{s}} = \frac{1}{2} \delta_s^2 K_s = \frac{1}{2} \delta_s f_s \tag{19}$$

where f_{n} is the normal force, f_s is the shear force, δ_t is the unload/reload displacement, δ_s is the shear displacement, K_t is the unload/reload spring stiffness ($K_t = E_r K^n$), and K_s is the shear spring stiffness.

The dissipated energy is a measure of how much energy has been lost, which is only known in an incremental sense. The dissipated energy for the shear and rotational mechanisms is the rectangular area under the force–displacement curve, as shown in Fig. 2d, for the case where the entire step is in the limit range. For the case where the load step includes both elastic and limit states, as in Fig. 2e, the step is broken into the elastic and limits increments.

For the normal load increment shown in Fig. 2b, the dissipated energy is thus given by:

$$E_{\text{Diss}}^{\text{n}} = \frac{1}{2} \left(f_{\text{n}}^2 - f_{\text{n}}^1 \right) \left(\delta_{\text{n}}^2 - \delta_{\text{n}}^1 \right) + f_{\text{n}}^1 \left(\delta_{\text{n}}^2 - \delta_{\text{n}}^1 \right), \quad \delta_{\text{n}}^2 > \delta_{\text{n}}^1 \tag{20}$$

where f_{n}^2 is the updated normal force, f_{n}^1 is the previous normal force, δ_{n}^2 is the updated normal displacement, and δ_{n}^1 is the previous normal displacement. The dissipated energy due to the normal mode can also be called the collisional mode.

The dissipated energy for the shear mode is determined differently for when the shear force (f_s) is beyond the limiting friction force (Fig. 2d) or below that force (Fig. 2e) and expressed as:
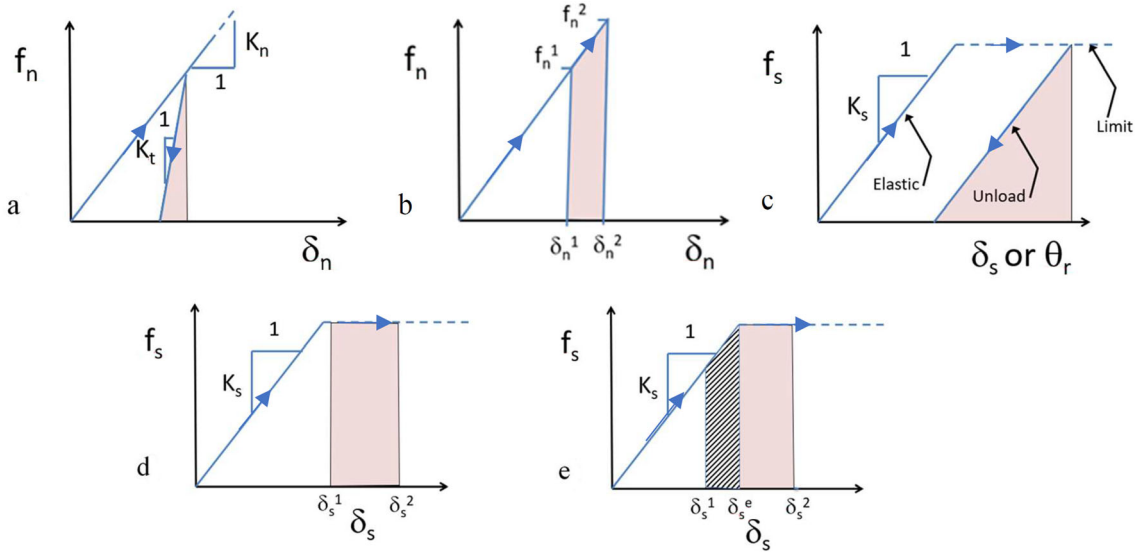
Fig. 2 Force–displacement curves for various types of particle contacts. **a** Stored normal energy. **b** Dissipated normal energy. **c** Stored shear and rotational energy. **d** Dissipated shear energy exceeding elastic limit. **e** Dissipated shear energy less than elastic limit

$$E_{\text{Diss}}^{\text{s}} = \begin{cases} f_{\text{limit}}\left(\delta_s^2 - \delta_s^1\right), & \delta_s^1 > \delta_s^{\text{e}} \\ \frac{1}{2}\left(f_{\text{limit}} - f_s^1\right)\left(\delta_s^{\text{e}} - \delta_s^1\right) + f_s^1\left(\delta_s^{\text{e}} - \delta_s^1\right), & \delta_s^1 < \delta_s^{\text{e}} \end{cases}$$

$$(21)$$

where f_{limit} is the limiting friction force, δ_s^2 is the updated shear displacement, δ_s^1 is the previous shear displacement, and δ_s^{e} is the elastic limit of the displacement. The second part of Eq. (21) is for unloading of the contact. The energy dissipated for the rolling mode is determined similarly by:

$$E_{\text{diss}}^{\text{r}} = M_{\text{c}}^{\text{r}}\theta_s \tag{22}$$

where M_{c}^{r} is the contact moment due to rolling, as shown in Eq. (15), and θ_s is the rotation of the particle.

The intent of damping for most DEM simulations is to reach a nearly static state. In this study, the contact laws accomplish this by including both hysteretic and viscous damping components. The viscous damping force is only applied during the unload-reload portion of the response in lieu of adding a complex hysteretic damping model. The dissipated energy due to damping for the normal and shear modes are calculated by:

$$E_{\text{damp}}^{\text{n}} = \frac{1}{2}\left(\delta_n^2 - \delta_n^1\right)f_{\text{damp}}^{\text{n}} \tag{23}$$

$$E_{\text{damp}}^{\text{s}} = \frac{1}{2}\left(\delta_s^2 - \delta_s^1\right)f_{\text{damp}}^{\text{s}} \tag{24}$$

where $f_{\text{damp}}^{\text{n}}$ is the normal component of the damping force and $f_{\text{damp}}^{\text{s}}$ is the shear component of the damping force. The damping forces, $f_{\text{damp}}^{\text{n}}$ and $f_{\text{damp}}^{\text{s}}$, are functions of a predefined damping factor and the rate of displacement for the contact.

3 Numerical model

For the numerical model, a confined system of particles was simulated under a shear loading condition. The initial configuration, shown in Fig. 1, includes 17,500 particles of various sizes consolidated by a vertical confining pressure of 700 kPa. The system is sheared by applying a pre-determined velocity to the top layer of particles for up to 25% shear strain. The system was created by consolidating 2500 particles with 200 μm radius, 5000 particles with 150 μm radius, and 10,000 particles with 100 μm radius. Table 1 shows the contact parameters used in the DEM simulations.

The applied velocity conditions are illustrated in Fig. 1. After compression, the top-most group of particles is

Table 1 DEM parameters used in simulations

Property	Units	Base value
Normal stiffness (K_N)	N/m	12,000
Shear stiffness (K_S)	N/m	2400
Rolling stiffness (K_R)	N/m	1.0E−2
Torsional stiffness (Km_t)	N/m	1.0E−2
Energy dissipation factor (E_R)	–	2.0
Inter-particle friction (μ_p)[a]	–	0.4
Rolling friction (μ_r)[a]	–	0.4
Initial height (H)	mm	10
Initial length (L)	mm	10
Initial width (w)	mm	3.5

[a]The inter-particle friction and rolling friction are varied with ranges from 0 to 0.8

rigidly displaced with a defined velocity to create the shear deformation. Similarly, the bottom-most particles are constrained to have zero horizontal velocity. Periodic boundary conditions are used in the horizontal direction. Both the top and bottom boundaries can move vertically to permit volume change. In addition to monotonic loading, cyclic loading simulations were conducted in which the system was strained to ± 20% strain for up to 1000 cycles.

4 Results and discussion

To study the internal consistency of the model, first the slip friction was determined for the base values shown in Table 1. The consistency of the energy calculations was verified by plotting the energy input along with the energy output. After this step, a parametric study was completed on the rolling resistance friction (μ_r) and the inter-particle friction (μ_p). Following this, a rate dependence study was completed to see if the system exhibited a velocity strengthening or weakening behavior. To better visualize the causes of the frictional behavior, each mode of energy was analyzed for varying inter-particle friction and applied strain rate. The study was concluded by looking at the effects of cyclically loading the system.

To demonstrate that energy balance is achieved by Eqs. (18–24), the total energy input to the system and the total energy output from the system were compared as seen in Fig. 3. The input energy was calculated by determining the forces and displacements of the top layer of particles that had a prescribed boundary condition, and the total output energy was a summation of the dissipated energy, which is the sum of hysteretic and viscous damping energy. Note that the stored energy component was negligible in these experiments, so the stored energy is not shown in Fig. 3. A similar procedure to determine input energy was used by Vora and Morgan [59]. As seen, the total energy
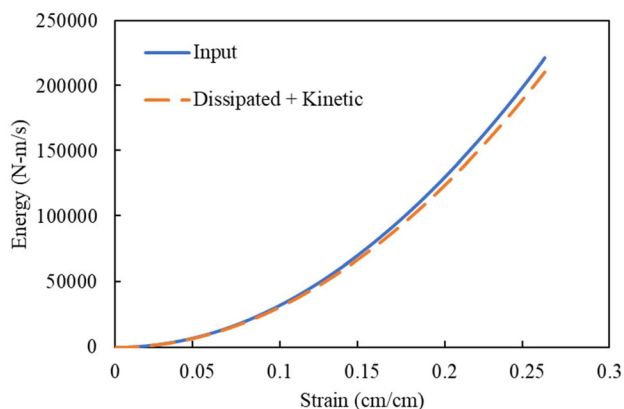
input to the system is equal to the total energy out of the system. This step was important to verify that the energy calculations were implemented correctly, and additionally shows that the DEM model is accurately determining the specified energies. After verifying the dissipated energy, the macroscopic friction was determined using Eq. (6).

Figure 4 shows the slip friction for an inter-particle sliding friction value of 0.4 and demonstrates the oscillatory nature of the slip interactions. The applied strain of 25% was sufficient for the slip friction of the system to reach a steady state. While the results are not presented here, a set of 2D and 3D simulations were performed up to 150% strain, which supported our reasoning for choosing 25% shear strain as the strain level where steady state is reached. Although, significant fluctuations may still occur once the peak stress has been reached. In Fig. 4, the slip friction shows a steady behavior after about 5% strain, where it begins to oscillate as for a stick–slip behavior. The oscillations are attributed to the formation and breakdown of force chains within the shear zone. The strain is computed based on the entire specimen length; however, the shearing occurs in a small zone roughly 10–12 particles in length.

The total macroscopic friction, μ_e, was calculated using Eq. (6) and is shown in Fig. 5. As can be seen, the mean friction value is around 0.54, which is reasonable when compared to values for sands under simple shear tests [65], where the data showed a constant value of 0.575. Interestingly, the value for friction using this macroscopic approach is much lower than the slip friction. This can be explained by calculating the dilative friction component. To further investigate this, multiple simulations were completed for different rolling resistance frictions and inter-particle frictions. The first DEM parameter to be studied was the rolling resistance friction (μ_r). The results for this study are shown in Fig. 6. The study for μ_r was completed for two different values of inter-particle friction, 0.2 and 0.4.
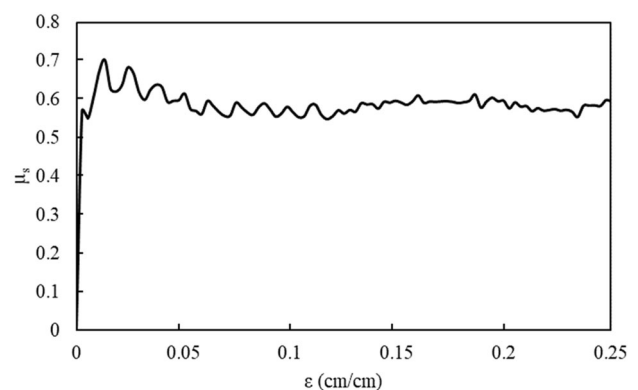

Fig. 3 Comparison of the total input energy and the total output energy of the system of particles to show conservation of energy

Fig. 4 Time evolution of slip friction with applied strain

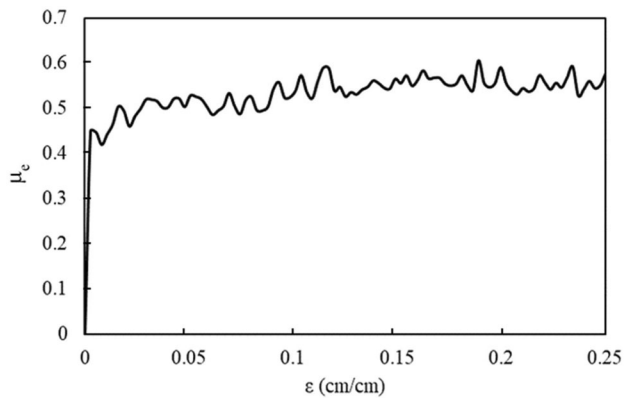**Fig. 5** Coefficient of friction by energy dissipation versus strain. The coefficient of friction μ_e was calculated using Eq. (6)

Fig. 7 Mean slip friction (μ_s), macroscopic friction (μ_e), and the dilative friction (μ_d) as a function of the inter-particle friction (μ_p)

As can be seen in Fig. 6, the value of slip friction (μ_s) quickly saturates to a steady value from $\mu_r = 0.1$ to $\mu_r = 0.8$. At zero rolling friction, the value of slip friction drops considerably. The effect of rolling friction can be seen by the fact that the slip friction increases going from a value of $\mu_r = 0.0$ to $\mu_r = 0.1$. The contribution of the rolling friction is somewhat substantial depending on μ_p. For example, with $\mu_p = 0.4$ and $\mu_r = 0.0$, the slip friction is nearly half of the value for μ_s at $\mu_r > 0.1$. However, increasing μ_r any more than 0.1 does not affect the frictional behavior.

Next, the inter-particle friction parameter was investigated for both slip friction (μ_s) and macroscopic friction (μ_e). By changing the value of inter-particle friction (μ_p), the slip friction of the system, determined by Eq. (1), can be varied dramatically, as seen in Fig. 7, which shows the strong dependence of the sliding friction of the system on the friction between individual particles.

Interestingly, μ_e remains nearly constant across the array of inter-particle friction values. Binaree et al. [3] found that the effective macroscopic friction saturates as the local (inter-particle) friction is increased. Additionally, Huang
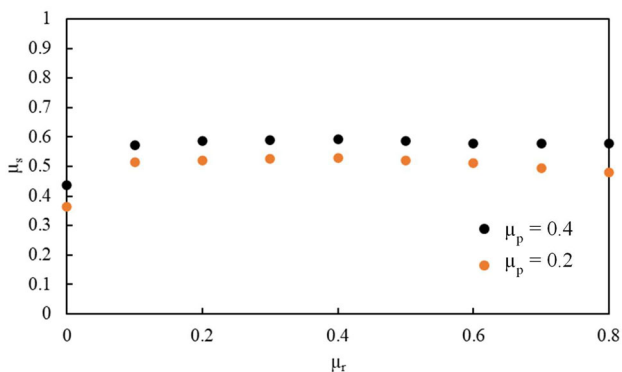

Fig. 6 Slip friction (μ_s) as a function of rolling resistance friction (μ_r) for two values of inter-particle friction (μ_p)
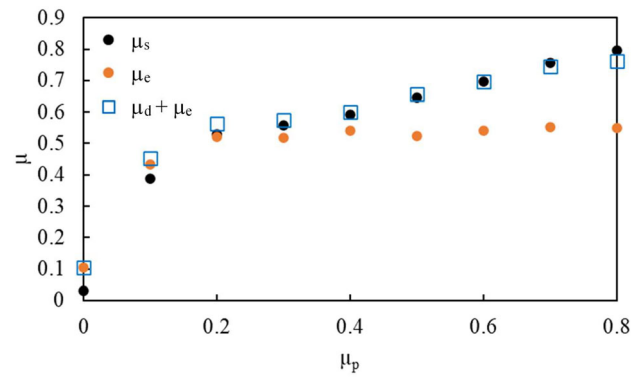
et al. [18] found that the sliding mode is affected drastically at lower values of μ_p, but the effect diminishes at higher levels of μ_p. Figure 7 shows that the macroscopic frictional behavior is not affected very much by changing the inter-particle friction. A possible explanation for this behavior is that once the inter-particle friction is high enough to form stable force chains, increasing it any further does not increase the stability of the chain, therefore does not increase the friction. The trends for the mean slip friction, macroscopic friction, and dilative friction are similar to those behaviors by Kruyt and Rothenbrug [27], for the peak shear strength, the steady-state shear strength, and the dilatancy rate. Also, at zero inter-particle friction, μ_s is a non-zero value around 0.05 for the 3D case, even though there is no sliding resistance. Therefore, the remaining resistance comes from the normal forces, via the contact moments. Another example of this interpretation is from the particle collision interactions noted by Peyneua and Roux [41], where frictionless bead packs showed macroscopic friction due to collisional interactions. It is noted that energy is dissipated by collisional contacts even when the particles are frictionless.

As shown in Eq. (7), the difference between μ_s and μ_e is the dilative friction, as shown in Fig. 7 by summing μ_s and μ_d. As shown for $\mu_p = 0.0$, the system showed very little compression or dilation; therefore, μ_s is approximately equal to μ_e. Figure 7 implies that increasing the inter-particle friction causes an increase in the dilation of the system. The dilative component of friction is non-dissipative; it increases the resistance to shear by performing work against the normal stress rather than dissipation at particle contacts. In traditional soil mechanics terminology, the friction must be *corrected* for dilation [64]. This becomes of great importance if the interest is computing heat loss because the dilative component of resistance does not generate heat. Using the DEM eliminates the need to separate out the apparent friction (that includes dilation)

from the true friction when working at the particle-scale behavior.

Figure 8 shows the effects of strain rate on friction. By changing the applied velocity of the selected region of particles at the top of the domain, the strain rate of the system can be varied. For lower values of inter-particle friction (μ_p), the mean slip friction shows little to no change with increasing strain rate. In fact, it shows a slight velocity-weakening behavior. However, as the inter-particle friction is increased, a velocity-strengthening behavior can be observed, and with further increase in inter-particle friction, the increase in mean slip friction with increasing strain rate is even more drastic. This type of behavior is similar to that of the frictional behavior in fault slip, where at very high rates of fault slip, the friction coefficient was shown to increase [43].

The weakening and strengthening of the system, shown in Fig. 8, can be explained because at lower inter-particle friction values, the particles cannot hold the force chains. The weakening and strengthening of the system, shown in Fig. 8, can be explained by the role of force chains. At lower inter-particle friction values, the particles cannot hold the force chains because the normal forces must make angles with the contact normals less than the particle friction angle to be stable. That is, the force resultants must lie within the so-called friction cone. Contacts are stable only if the contact force is nearly aligned with the contact normal. However, when the friction is increased, the friction cones expand making it easier to create stable contacts, thus allowing more force chains to form. Once a large portion of the contacts are stable, increasing the friction does not proportionately increase the number of stable contacts. The increased force chain formation contributes to the large increase in friction as the rate is increased, shown in Fig. 8. Despite the microscale friction coefficients being independent of rate, Fig. 8 shows that
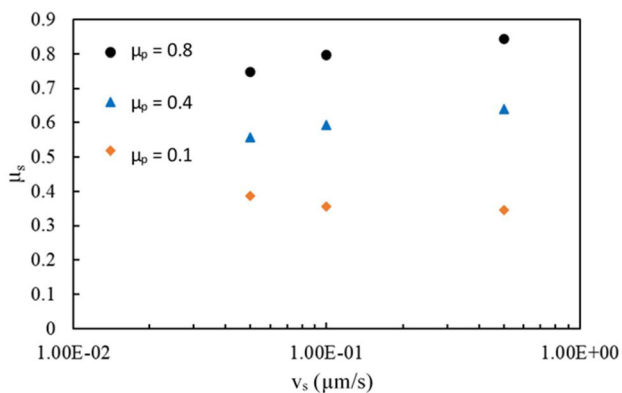
the model captures the rate effect on the macroscale frictional behavior.

Figure 9 visualizes the formation and break down of force chains by showing the progression of maximum principal stress for each particle at various strains. As seen in Fig. 9, strain localization is observed in a small subset of particles near the top boundary. However, the strain localization does not invalidate the key contribution of this study, which is establishing a link between the dissipated energy measured at the microscale and that observed at the macroscale. The principles employed in this study for calculating different components of energy dissipation are valid in the presence of complex strain patterns including localization.

Each mode of dissipated energy (shear, rolling, and normal) was then analyzed by normalizing the value by the total dissipated energy. Three different values of inter-particle friction were studied as shown in Fig. 10. As shown, for the lowest value of inter-particle friction, Fig. 10a, the dissipated energy is dominated by the normal collisional energy, as expected, and then as the inter-particle friction is increased the shear and normal components seem to settle out to average values around 0.4 and 0.6, respectively, with very little rotational components. Although the contribution of the rotational resistance to the energy dissipation is small, the rotational resistance plays a large role in stabilizing the force chains.

The different modes of dissipated energy were analyzed for varying applied shear rates (Fig. 11). Interestingly, as the applied strain rate was increased, the amount of dissipated energy for the shear mode decreased and the normal mode conversely increased. The average value for shear dissipation decreased from 0.45 to 0.25, where the normal dissipation increased from 0.55 to 0.7. The rolling component seemed to vary. These results suggest the normal (collisional) mode is responsible for the drastic increase in macroscopic friction behavior seen in Fig. 8. It should be noted that the normal mode would provide resistance even if the shear component is small, similar to how frictionless particles can resist the shear as seen in Figs. 6–7. The results presented in Fig. 11 were obtained for the given set of parameters. The contribution of each component of energy dissipated may change based on particle shape, particle stiffness, particle contact law, and the rate of loading, among others. For instance, energy dissipation by normal contacts is probably greatest in spheres whereas non-spherical particles may exhibit a different behavior. Whereas the application is demonstrated for one set of loading conditions and particle properties, the presented methodology can be used for different particle attributes.

Cyclical simulations were completed where the system was strained to values of ± 20% strain for N number of cycles. Figure 12 shows the resulting coefficient of friction

Fig. 8 Mean slip friction as a function of the velocity in the horizontal direction (v_s) for varying inter-particle friction (μ_p) values of 0.1, 0.4, and 0.8
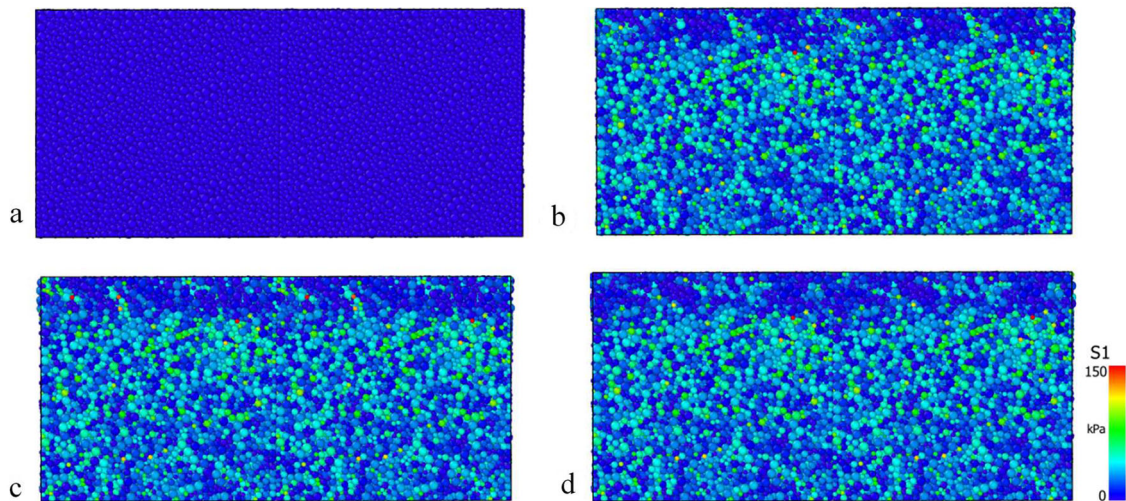
Fig. 9 Maximum principal stress for each particle at **a** 0% strain, **b** 5% strain, **c** 15% strain, and **d** 20% strain. Note that the stress shown is in kPa, and this is for a slice of the 3D domain
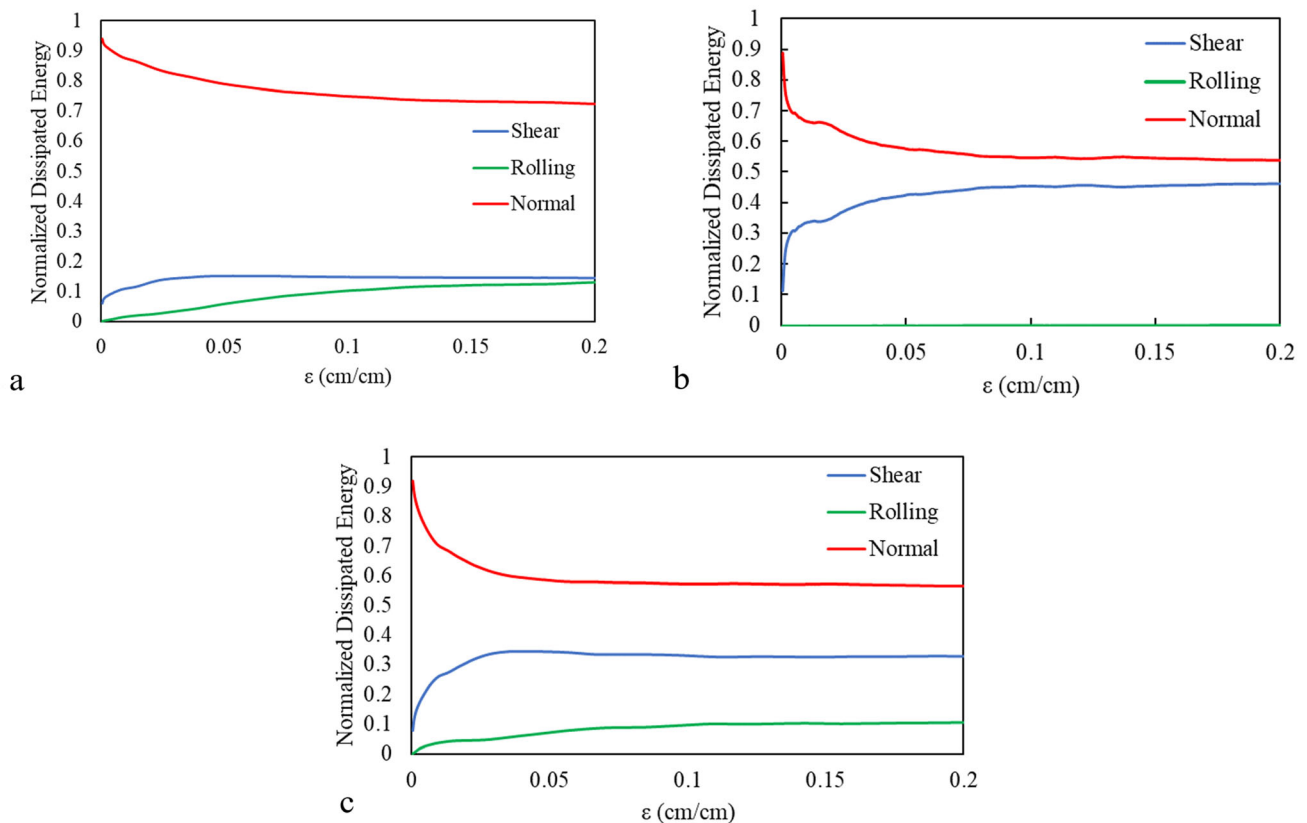

Fig. 10 Different modes of dissipated energy normalized by the total dissipated energy for **a** $\mu_p = 0.3$, **b** $\mu_p = 0.6$, and **c** $\mu_p = 0.8$

versus the number of steps for an inter-particle friction value of 0.6. For the cyclical simulations, the coefficient of friction averages to 0.24, where the normally loaded system was 0.25 for the same properties. The breaking and reforming of the force chains is evident in the oscillatory nature of the plot. For example, as the particles reach +

20% strain, the loading is then reversed resulting in the breaking of load resisting force chains that were formed. Then, the particles begin to form new force chains that resist the new motion.

In this study, the Taylor model [52] was used because it is both simple and has historical context. Based on the
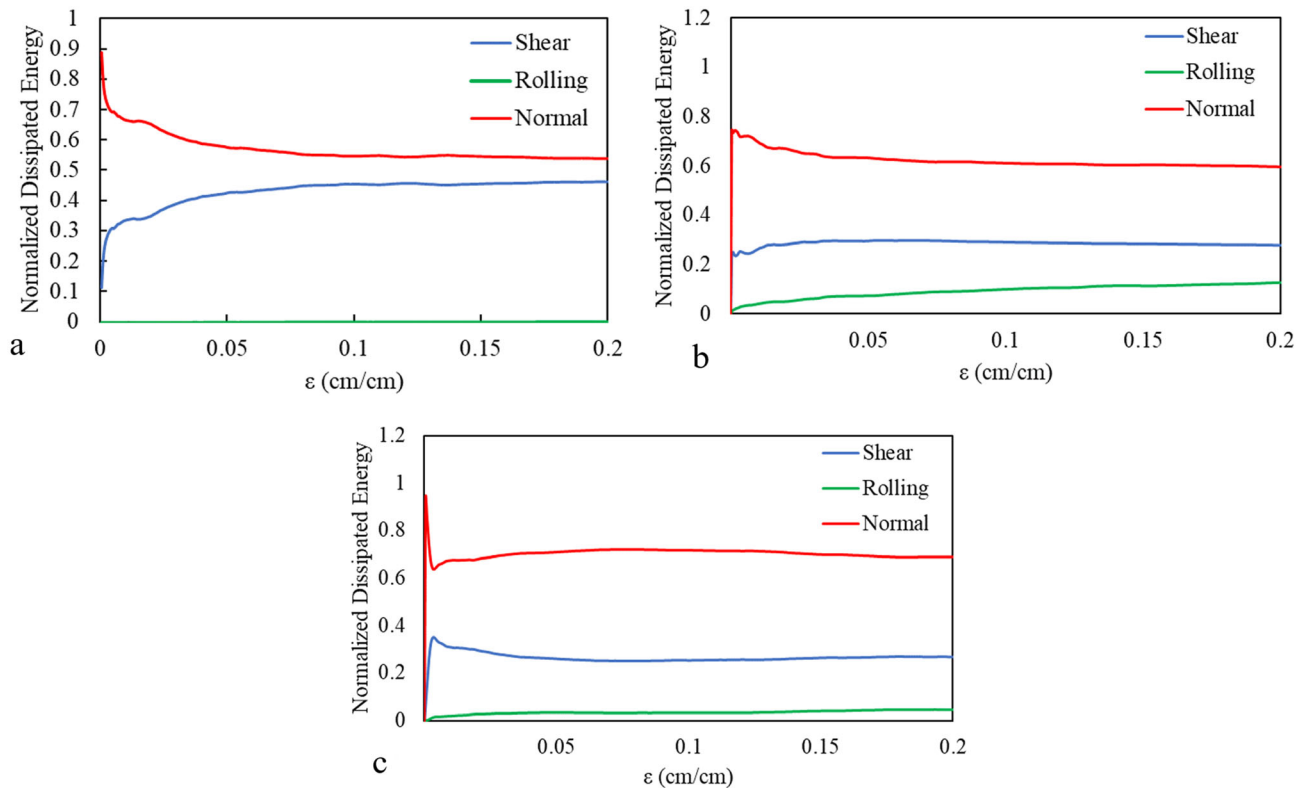
Fig. 11 Different modes of dissipated energy normalized by the total dissipated energy for **a** $v_s = 0.1$ μm/s, **b** $v_s = 5$ μm/s, and **c** $v_s = 10$ μm/s
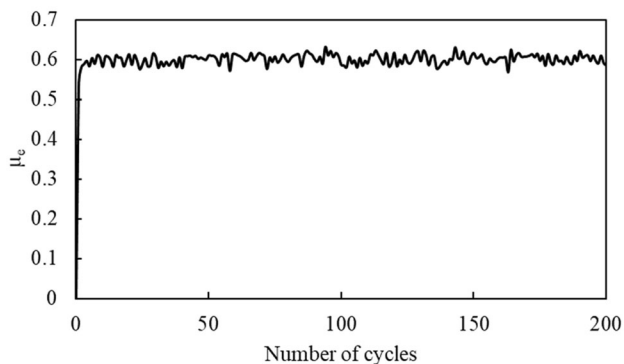

Fig. 12 Coefficient of friction versus number of cycles for $\mu_p = 0.6$ for 200 cycles

results of this study, the Taylor method is also consistent with the micro-scale model presented, which is likewise simple and lacks provision for particle shapes, contact degradation, and particle breakage.

5 Conclusion

Energy dissipated in a granular layer subjected to monotonic and cyclic simple shear loading was investigated based on DEM simulations. The simulations results were interpreted in the context of traditional Critical State Soil Mechanics but using internally measured energies. Independent computation of internal energy dissipation using the DEM inter-particle contact laws is a unique contribution that allows the internal consistency of the model to be investigated. In is also the first step in a thermal analysis of the granular layer during shear. In addition, the individual contribution of dissipation mechanism to the total energy budget could be assessed. The simulation results showed that the macroscopic friction, determined from internal energy dissipation, was essentially constant throughout loading and differed from the slip friction by an amount equal to the non-energy dissipating dilatancy component. Thus, the use of internally computed energies obviates the need to remove the dilatancy component of resistance. The results also showed that although a small amounts of inter-particle rolling and sliding friction resistances are needed in the DEM model, there are threshold values beyond which increasing neither the rolling resistance parameter nor the inter-particle sliding friction affected the macroscopic friction. These observations suggest that forces are applied through contiguous chains of particles, favoring energy dissipation through the collisional mode of particle interaction. A study on applied strain rate showed that the macroscopic friction increased for higher values of applied velocity. The framework presented in this study can be extended to include non-spherical grains and more

complex contact laws, including contact bonding, degradation of contacts and particle breakage. Further, the proposed model can be coupled to multiphysics solvers in future studies to describe the frictional behavior of granular media subject to processes including heat transfer, fluid flow, and chemical interactions.

References

1. Annunziata MA, Baldassarri A, Dalton F, Petri A, Pontuale G (2016) Increasing 'ease of sliding' also increases friction: when is a lubricant effective? J Phys Condens Matter 28(13):134001

2. Asteriou P, Saroglou H, Tsiambaos G (2012) Geotechnical and kinematic parameters affecting the coefficients of restitution for rock fall analysis. Int J Rock Mech Min Sci 54:103–113

3. Binaree T, Azéma E, Estrada N, Renouf M, Preechawuttipong I (2020) Combined effects of contact friction and particle shape on strength properties and microstructure of sheared granular media. Phys Rev E 102(2):022901

4. Brantut N, Schubnel A, Rouzaud JN, Brunet F, Shimamoto T (2008) High-velocity frictional properties of a clay-bearing fault gouge and implications for earthquake mechanics. J Geophys Res Solid Earth 113(B10): B10401

5. Brown E, Jaeger HM (2012) The role of dilation and confining stresses in shear thickening of dense suspensions. J Rheol 56(4):875–923

6. Campbell CS, Cleary PW, Hopkins M (1995) Large-scale landslide simulations: global deformation, velocities and basal friction. J Geophys Res Solid Earth 100(B5):8267–8283

7. Chen J, Niemeijer AR, Spiers CJ (2017) Microphysically derived expressions for rate-and-state friction parameters, a, b, and Dc. J Geophys Res Solid Earth 122(12):9627–9657

8. Clark JI, Meyerhof GG (1972) The behavior of piles driven in clay. I. An investigation of soil stress and pore water pressure as related to soil properties. Can Geotech J 9(4):351–373

9. Cui L, O'Sullivan C (2006) Exploring the macro-and micro-scale response of an idealised granular material in the direct shear apparatus. Geotechnique 56(7):455–468

10. Cundall PA, Strack OD (1979) A discrete numerical model for granular assemblies. Geotechnique 29(1):47–65

11. Van den Ende MPA, Chen J, Ampuero JP, Niemeijer AR (2018) A comparison between rate-and-state friction and microphysical models, based on numerical simulations of fault slip. Tectonophysics 733:273–295

12. Van den Ende M, Marketos G, Niemeijer AR, Spiers CJ (2015) A microphysical interpretation of rate-and-state friction behaviour:insights from discrete element modelling. In: AGU fall meeting abstracts, 2015 AGUFMMR33A2646V

13. Gao K, Euser BJ, Rougier E, Guyer RA, Lei Z, Knight EE, Carmeliet J, Johnson PA (2018) Modeling of stick-slip behavior in sheared granular fault gouge using the combined finite-discrete element method. J Geophys Res Solid Earth 123(7):5774–5792

14. Geller DA, Ecke RE, Dahmen KA, Backhaus S (2015) Stick-slip behavior in a continuum-granular experiment. Phys Rev E 92(6):060201

15. Gomberg J, Beeler N, Blanpied M (2000) On rate-state and Coulomb failure models. J Geophys Res Solid Earth 105(B4):7857–7871

16. Gu DM, Huang D, Liu HL, Zhang WG, Gao XC (2019) A DEM-based approach for modeling the evolution process of seepage-induced erosion in clayey sand. Acta Geotech 14(6):1629–1641

17. Hanley KJ, Huang X, O'Sullivan C (2017) Energy dissipation in soil samples during drained triaxial shearing. Géotechnique 68(5):421–433

18. Huang X, Hanley KJ, O'Sullivan C, Kwok CY (2014) Exploring the influence of interparticle friction on critical state behaviour using DEM. Int J Numer Anal Meth Geomech 38(12):1276–1297

19. Hungr O (1995) A model for the runout analysis of rapid flow slides, debris flows, and avalanches. Can Geotech J 32(4):610–623

20. Ikari MJ, Carpenter BM, Marone C (2016) A microphysical interpretation of rate-and state-dependent friction for fault gouge. Geochem Geophys Geosyst 17(5):1660–1677

21. Iwashita K, Oda M (1998) Rolling resistance at contacts in simulation of shear band development by DEM. J Eng Mech 124(3):285–292

22. Jiang S, Shen L, Guillard F, Einav I (2020) The effect of cement material properties on the fracture patterns developing within cement-covered brittle sphere under impact. Acta Geotech 16:1–11

23. Johnson PA, Jia X (2005) Nonlinear dynamics, granular media and dynamic earthquake triggering. Nature 437(7060):871

24. Johnson PA, Savage H, Knuth M, Gomberg J, Marone C (2008) Effects of acoustic waves on stick–slip in granular media and implications for earthquakes. Nature 451(7174):57

25. Johnson DH, Vahedifard F, Jelinek B, Peters JF (2017) Micromechanical modeling of discontinuous shear thickening in granular media-fluid suspension. J Rheol 61(2):265–277

26. Kasyap SS, Senetakis K, Coop MR, Zhao J (2020) Micromechanical behaviour in shearing of reproduced flat LBS grains with strong and weak artificial bonds. Acta Geotech 16:1–22

27. Kruyt NP, Rothenburg L (2006) Shear strength, dilatancy, energy and dissipation in quasi-static deformation of granular materials. J Stat Mech Theory Exp 2006(07):P07021

28. Kwok CY, Duan K, Pierce M (2020) Modeling hydraulic fracturing in jointed shale formation with the use of fully coupled discrete element method. Acta Geotech 15(1):245–264

29. Liu J, Lv P, Cui Y, Liu J (2014) Experimental study on direct shear behavior of frozen soil–concrete interface. Cold Reg Sci Technol 104:1–6

30. Lucas A, Mangeney A, Ampuero JP (2014) Frictional velocity-weakening in landslides on Earth and on other planetary bodies. Nat Commun 5:3417

31. Luding S (1997) Stress distribution in static two-dimensional granular model media in the absence of friction. Phys Rev E 55(4):4720

32. Marone C, Raleigh CB, Scholz CH (1990) Frictional behavior and constitutive modeling of simulated fault gouge. J Geophys Res Solid Earth 95(B5):7007–7025

33. Matsushima T (2005) Effect of irregular grain shape on quasi-static shear behavior of granular assembly. Powders Grains P&G05 2:1319–1323

34. Mirghasemi AA, Rothenburg L, Matyas EL (2002) Influence of particle shape on engineering properties of assemblies of two-dimensional polygon-shaped particles. Geotechnique 52(3):209–217

35. Morgan JK (2004) Particle dynamics simulations of rate-and state-dependent frictional sliding of granular fault gouge. In:

Computational earthquake science part I. Birkhäuser, Basel, pp 1877–1891

36. O'Brien JS, Julien PY, Fullerton WT (1993) Two-dimensional water flood and mudflow simulation. J Hydraul Eng 119(2):244–261

37. Oda M, Iwashita K (2000) Study on couple stress and shear band development in granular media based on numerical simulation analyses. Int J Eng Sci 38(15):1713–1740

38. Oron G, Herrmann HJ (1998) Exact calculation of force networks in granular piles. Phys Rev E 58(2):2079

39. Peters JF, Jelinek B, Goodman CC, Vahedifard F, Mason GL (2019) Large scale discrete-element modeling for engineering analysis: acase study for the mobility cone penetrometer. J Geotech Geoenviron Eng. 145(12):04019111

40. Peters JF, Muthuswamy M, Wibowo J, Tordesillas A (2005) Characterization of force chains in granular material. Phys Rev E 72(4):041307

41. Peyneau PE, Roux JN (2008) Frictionless bead packs have macroscopic friction, but no dilatancy. Phys Rev E 78(1):011307

42. Potyondy JG (1961) Skin friction between various soils and construction materials. Geotechnique 11(4):339–353

43. Rice JR (2006) Heating and weakening of faults during earthquake slip. J Geophys Res Solid Earth 111(B5):B05311

44. Rothenburg L, Bathurst RJ (1992) Micromechanical features of granular assemblies with planar elliptical particles. Geotechnique 42(1):79–95

45. Sandeep CS, Senetakis K, Cheung D, Choi CE, Wang Y, Coop MR, Ng CWW (2021) Experimental study on the coefficient of restitution of grain against block interfaces for natural and engineered materials. Can Geotech J 58(1):35–48

46. Savage SB, Hutter K (1989) The motion of a finite mass of granular material down a rough incline. J Fluid Mech 199:177–215

47. Schofield A, Wroth P (1968) Critical state soil mechanics, vol 310. McGraw-Hill, London

48. El Shamy U, Denissen C (2012) Microscale energy dissipation mechanisms in cyclically-loaded granular soils. Geotech Geol Eng 30(2):343–361

49. Skinner AE (1969) A note on the influence of inter-particle friction on the shearing strength of a random assembly of spherical particles. Geotechnique 19(1):150–157

50. Suiker AS, Fleck NA (2004) Frictional collapse of granular assemblies. J Appl Mech Trans ASME 71(3):350–358

51. Tao H, Tao J (2017) Quantitative analysis of piping erosion micro-mechanisms with coupled CFD and DEM method. Acta Geotech 12(3):573–592

52. Taylor DW (1948) Fundamentals of soil mechanics. Soil Sci 66(2):161

53. Thornton C (1997) Coefficient of restitution for collinear collisions of elastic-perfectly plastic spheres. J Appl Mech 64:383–386

54. Thornton C (2000) Numerical simulations of deviatoric shear deformation of granular media. Géotechnique 50(1):43–53

55. Tinti E, Spudich P, Cocco M (2005) Earthquake fracture energy inferred from kinematic rupture models on extended faults. J Geophys Res Solid Earth 110(B12):B12303

56. Tomac I, Gutierrez M (2017) Coupled hydro-thermo-mechanical modeling of hydraulic fracturing in quasi-brittle rocks using BPM-DEM. J Rock Mech Geotech Eng 9(1):92–104

57. Tsubakihara Y, Kishida H (1993) Frictional behaviour between normally consolidated clay and steel by two direct shear type apparatuses. Soils Found 33(2):1–13

58. Vagnon F, Pirulli M, Manzella I, Kelfoun K, Ferrero AM, Goebert S, Treadgold R, Boon D, Squires P, Courtman S, Endacott R (2018) Numerical analysis of the rheological behaviour of the Socompa debris avalanche, Chile. In: Geomechanics and geodynamics of rock masses: selected papers from the 2018 European rock mechanics symposium. CRC Press, p 409

59. Vora HB, Morgan JK (2019) Microscale characterization of fracture growth and associated energy in granite and sandstone analogs: insights using the discrete element method. J Geophys Res Solid Earth. https://doi.org/10.1029/2019JB018155

60. Walton IO, Braun RL (1986) Stress calculations for assemblies of inelastic speres in uniform shear. Acta Mech 63(1):73–86

61. Wang P, Arson C (2018) Energy distribution during the quasi-static confined comminution of granular materials. Acta Geotech 13(5):1075–1083

62. Wang J, Yan H (2012) DEM analysis of energy dissipation in crushable soils. Soils Found 52(4):644–657

63. Weber B, Suhina T, Brouwer AM, Bonn D (2019) Frictional weakening of slip interfaces. Sci Adv 5(4):eaav7603

64. Wood DM (2002) Constitutive cladistics: the progeny of critical state soil mechanics. In: Constitutive and centrifuge modelling: two extremes: proceedings of the workshop on constitutive and centrifuge modelling, Monte Verità, Switzerland, 8–13 July 2001. CRC Press, p 35

65. Wood DM (1990) Soil behaviour and critical state soil mechanics. Cambridge University Press

66. Xiao Y, Yuan Z, Chu J, Liu H, Huang J, Luo SN, Wang S, Lin J (2019) Particle breakage and energy dissipation of carbonate sands under quasi-static and dynamic compression. Acta Geotech 14(6):1741–1755

67. Yavari N, Tang AM, Pereira JM, Hassen G (2016) Effect of temperature on the shear strength of soils and the soil–structure interface. Can Geotech J 53(7):1186–1194

68. Zhai C, Herbold EB, Hall SA, Hurley RC (2019) Particle rotations and energy dissipation during mechanical compression of granular materials. J Mech Phys Solids 129:19–38

69. Zhang W, Wang J, Jiang M (2013) DEM-aided discovery of the relationship between energy dissipation and shear band formation considering the effects of particle rolling resistance. J Geotech Geoenviron Eng 139(9):1512–1527

70. Zong-Ze Y, Hong Z, Guo-Hua X (1995) A study of deformation in the interface between soil and concrete. Comput Geotech 17(1):75–92